Renewable Energy 239 (2025) 122035

Contents lists available at ScienceDirect

Renewable Energy

journal homepage: www.elsevier.com/locate/renene

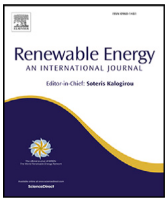

A novel metric for quantifying solar irradiance stability: Mapping solar irradiance variability to photovoltaic power generation

Qun Tian [a], Jinxiao Li [b], Zhiang Xie [c,*], Puxi Li [d], Ya Wang [e], Dongwei Chen [f], Yue Zheng [g]

[a] *Guangzhou Institute of Tropical and Marine Meteorology of China Meteorological Administration/Guangdong Provincial Key Laboratory of Regional Numerical Weather Prediction, GBA Academy of Meteorological Research, Guangzhou, 510641, China*

[b] *Shanghai Investigation, Design and Research Institute Co., Ltd., Shanghai, 200434, China*

[c] *Department of Earth and Space Sciences, Southern University of Science and Technology, Shenzhen, 518055, China*

[d] *State Key Laboratory of Severe Weather, Chinese Academy of Meteorological Sciences, China Meteorological Administration, Beijing, 100081, China*

[e] *State Key Laboratory of Numerical Modeling for Atmospheric Sciences and Geophysical Fluid Dynamics, Institute of Atmospheric Physics, Chinese Academy of Sciences, Beijing, 100029, China*

[f] *School of Mathematical and Statistical Sciences, Clemson University, Clemson, 29634, SC, USA*

[g] *ClusterTech Ltd., 999077, Hong Kong Special Administrative Region of China*

ARTICLE INFO

Keywords:
Photovoltaic
Solar irradiance
Solar instability index
Wasserstein distance

ABSTRACT

The daily stability of solar irradiance significantly influences photovoltaic (PV) power generation; however, existing metrics for assessing it normally fail to robustly correlate with daily PV output. To address this gap, we introduce a new metric, the solar instability index (SII), formulated by applying the Wasserstein distance to assess the deviation of intra-day solar irradiance pattern from the anticipated diurnal cycle. In our case station, SII closely correlates with atmospheric moisture and available solar energy, suggesting its strong association with synoptic weather events that lead to solar resource loss. We further scrutinize the efficacy of SII alongside two existing metrics through two case studies. The results demonstrate that SII excels in capturing low-frequency variations in solar irradiance without relying on arbitrarily assigned parameters, thereby outperforming the other two metrics in establishing a robust correlation with PV power output. As such, in scenarios involving site selection for PV power plant, SII stands as a valuable metric for assessing the potential stability of daily PV power generation.

1. Introduction

Solar irradiance on the Earth's surface is predominantly governed by two principal factors: the radiation reaching the top of the atmosphere, determined by solar brightness and the Earth's orbit parameters [1], and the reflection, scattering, and absorption effects of the atmosphere [2]. Since solar brightness and the orbital parameters of Earth remain nearly constant on a decade timescale [3,4], studies on solar irradiance variations typically concentrate on atmosphere-related factors. Within this scope, cloudiness stands as the primary driver of these variations, with features such as the spatial distribution, fraction of cloud cover, the intensity of convection processes, and the speed of advection significantly shaping the outcome [5,6]. Those cloud behaviors are intricately linked to synoptic weather events, including frontal systems, convective storms, and tropical cyclones [7]. Moreover, aerosols also substantially affect solar irradiance variability, particularly over large spatial and temporal scales [8,9]. Intense aerosol loads in the atmosphere due to dust storms, sandstorms, or pollution events lead to haze formation, causing concurrently decreased solar irradiance [6]. These atmosphere-related factors cause deviations in downwelling solar radiation from clear sky conditions at ground level, resulting in altered (mostly reduced) photovoltaic (PV) power generation.

Several established algorithms exist for quantifying solar irradiance stability. One type of commonly used algorithm involves the clear-sky index and clearness index, derived from the ratio of ground-level solar irradiance to the estimated value under clear sky conditions and the ratio of ground-level solar irradiance to extraterrestrial levels, respectively [10–13]. Increments of these indices, i.e., the difference between consecutive measurements, have been used to quantify solar irradiance stability through mean values, standard deviations, and other statistical properties [14–16]. Another type of method uses the sunshine number, a binary variable indicating whether the sun is covered based on a solar irradiance threshold [17]. Qualifiers such as the daily averaged sunshine stability number (DASSN), measuring the daily average value of positive increments of the sunshine number, have been developed to

---

* Corresponding author.
E-mail address: xieza@sustech.edu.cn (Z. Xie).

https://doi.org/10.1016/j.renene.2024.122035
Received 15 May 2024; Received in revised form 10 October 2024; Accepted 26 November 2024
Available online 6 December 2024
0960-1481/© 2024 Elsevier Ltd. All rights reserved, including those for text and data mining, AI training, and similar technologies.

List of abbreviations

Abbreviation	Definition
DARR	Daily aggregate ramp rate
DASSN	Daily averaged sunshine stability number
GHI	Global horizontal irradiance
PDF	Probability distribution function
PV	Photovoltaic
RH	Relative humidity
SII	Solar instability index

assess solar irradiance stability [17,18]. Additionally, metrics based on the increments of cloud properties derived from satellite imagery – such as the effective cloud cover coefficient – have also been established [19,20]. Regarding the irregularity of solar irradiance time series, researchers have also employed the fractal dimension as a quantifier of its variability [21,22]. Furthermore, algorithms combining these various quantifiers have been developed in the existing literature [23,24].

However, it can be deduced that these established metrics for measuring solar irradiance stability generally struggle to robustly correlate with solar energy generation, primarily due to their omission of key information. Atmosphere-related intra-day fluctuations in solar irradiance can be broadly categorized into two types: high-frequency fluctuations (referred to as type 1), occurring as broken clouds pass by, temporarily diminishing irradiance for seconds to one hour, and low-frequency fluctuations (type 2), occurring when large-scale clouds or haze persist, reducing irradiance for several hours. Previous studies (e.g., Refs. [24,25]) show that existing quantifiers are generally adept at dealing with type 1 but exhibit limited capability in capturing type 2. Consequently, fully overcast days are highly likely to be classified as stable using those quantifiers, owing to minor high-frequency fluctuations despite significant deviations from the anticipated diurnal cycle. However, under such conditions, the PV power output would be notably lower than expected based on the diurnal cycle, contradicting the classification. As such, it is insufficient to consider high-frequency fluctuations solely when measuring the stability of solar irradiance in the context of PV power generation. Additionally, the introduction of artificial criteria in some metrics (such as DASSN) could lead to fluctuations in their relationship with PV power output as the criteria change. Therefore, there is a need for a new metric to evaluate solar irradiance stability, one that is closely correlated with atmospheric processes occurring on various timescales that lead to a reduction in solar resource and, consequently, is robustly linked to PV power output.

The advancement of mathematical methodologies provides improved tools for assessing solar irradiance stability. A promising candidate is the Wasserstein distance. Rooted in optimal transport theory [26], this metric measures the optimal “effort” needed to transport mass between two probability distributions, enabling the quantification of differences between them [27–30]. Currently, the Wasserstein distance has been applied to various science fields, encompassing climate model evaluation [29], detection of synchronization in dynamical systems [31], and statistical parameter estimation [32]. It has also gained prominence in machine learning, particularly as a valuable tool for Generative Adversarial Networks [33–35]. In the case of quantifying solar irradiance stability, we employ the Wasserstein distance as a measure of distinctions between the temporal distribution of solar irradiance and a reference distribution and term this metric as the solar instability index (SII), where a higher value indicates a higher level of instability. Due to its mathematical feature, this new metric has the potential to capture both types of fluctuations and therefore establish a strong connection with PV power generation.

The present study is structured as follows. Section 2 offers an overview of the data used and presents the formal definition of SII and two other metrics for comparison. In Section 3, we first provide a case-based explanation of the functionality of SII to assist readers in building a better understanding of it. Subsequently, the daily evolution of SII over a year is outlined, followed by an exploration of the physical processes influencing it. A comparative analysis with existing metrics for SII is then conducted to highlight the unique insights the proposed metric provides. Finally, Section 4 summarizes key findings and offers commentary on SII and other relevant metrics.

2. Data and method

2.1. Data and preprocessing

The solar irradiance, air temperature, humidity, and power output data were collected from the Herun PV power plant (21.6°N, 111.4°E) in Guangdong, China. This power plant is located in the low-lying flat terrain along the southern coast of China (Fig. 1). It is situated within the monsoon region, characterized by dry conditions and prevailing northerly winds in winter and humid conditions with prevailing southerly winds in summer. The data covers the whole year of 2022 at 5-min intervals. Multiple quality check steps were performed to remove erroneous and suspicious records:

1. Remove records that exceed a reasonable range. After consulting the historical meteorological data, the range for global horizontal irradiance (GHI), temperature, and relative humidity (RH) is set as $0\sim1400$ W/m^2, $-40\sim60$ °C, and $0\sim100\%$, respectively. Since the power plant’s installed capacity is 50 MW and the power consumption of the PV module during operation is around 0.1 MW, the range for the power output is set as $-1\sim50$ MW.

2. Remove records that remain unchanged over a certain period. Considering the varying nature of the atmospheric environment, the non-varying observation records are most likely due to malfunctioning of the instruments and, therefore, should be removed. The threshold for GHI (power output) is 5 h for non-zero value records (equal or above zero value records) and 20 h for zero value records (below zero value records). For temperature and RH, the threshold is 5 h.

3. Remove records during maintenance. According to the operation and maintenance records of the power plant, the PV modules were manually shut down for maintenance three times with a total duration of 9 days in the year 2022. Data collected on these days were excluded from the analysis.

After quality control procedures, a total of 100,091 records were used in the subsequent analysis.

2.2. Method

The primary application of the Wasserstein distance is to quantify the disparity between two probability distribution functions (PDFs). Expressed as $\mathcal{W}_p(\mu,\nu)$ on $\mathbb{R}^d$, where $p\in[1,\infty)$ and $\pi\in\Pi(\mu,\nu)$ represents a joint distribution, the Wasserstein distance is mathematically formalized as:

$$\mathcal{W}p(\mu,\nu)=\left(\inf_{\pi\in\Pi(\mu,\nu)}\int_{\mathbb{R}^d\times\mathbb{R}^d}|x-y|^p\ d\pi(x,y)\right)^{\frac{1}{p}} \tag{1}$$

To contextualize this approach for assessing solar irradiance stability, we first treat intra-day solar irradiance patterns as PDFs by

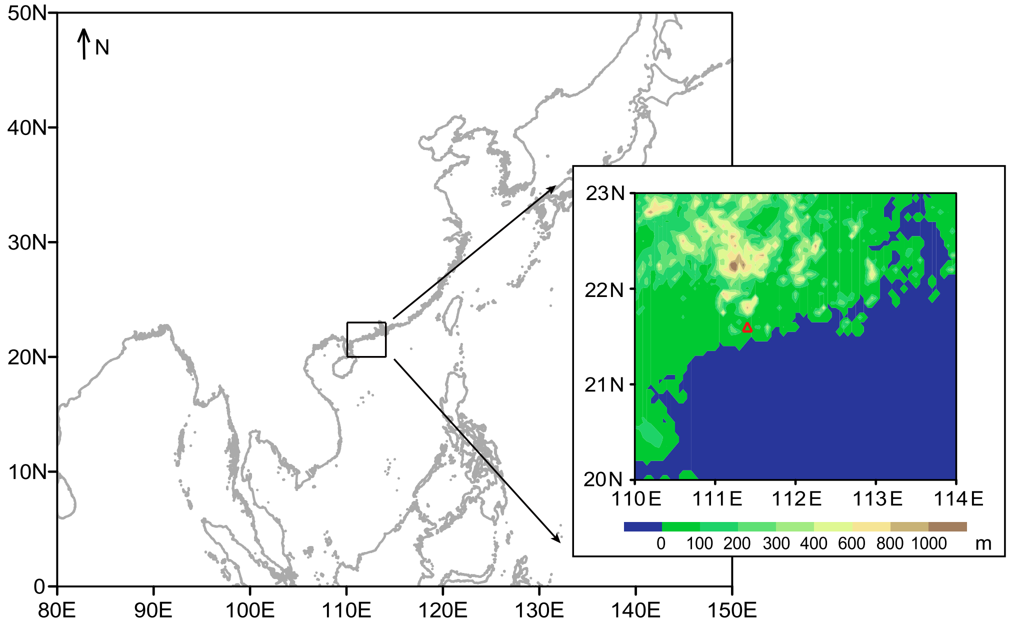

Fig. 1. Location (red triangle) and topography (shaded) of Herun photovoltaic power plant.

normalization (i.e., ensuring the integration of intra-day distribution as 1). This treatment enables the application of Wasserstein distance to assess the variability of these solar irradiance time series, regardless of changing solar elevation angles across the year. Second, given the prevalence of the diurnal cycle in governing intra-day variations in solar irradiance, we treat the diurnal cycle as PDF (also by normalization) and take it as a reference. Finally, the Earth Movement Distance ($p = 1$) is used, where the metric intuitively calculates the minimal "cost" required to transform one distribution into another. SII is denoted by:

$$SII = \inf_{\pi\in\Pi(\mu,\nu)} \int_{\mathbb{D}_G\times\mathbb{D}_r} \left|T_G - T_r\right| \, d\pi(T_G,T_r) \tag{2}$$

where μ and ν represent the PDFs for a given day and the reference, respectively. π stands for the joint distribution between those two PDFs, while T_G and T_r denote the hours from 12 p.m. during the given day ($\mathbb{D}_G$) and the reference ($\mathbb{D}_r$). Overall, this new metric provides a means to gauge the extent to which solar irradiance patterns deviate from the anticipated diurnal cycle, enabling a comprehensive assessment of solar irradiance stability. It is important to note that the temporal units used in this study (T_G and T_r) are hours, and the values of SII could vary if calculated using different temporal units.

Two commonly used quantifiers, daily aggregate ramp rate (DARR) and DASSN, were also computed to compare with SII. The DARR is defined as [36]:

$$DARR = \sum_{t=1}^{T-1} \frac{|G(t+1) - G(t)|}{C} \tag{3}$$

where $G(t)$ is the GHI, and C is an optional constant for normalization (set to 1 in this study, indicating that no normalization is applied). To exclude fluctuations associated with clock time, we substitute $G(t)$ with the clearness index $k_c(t)$, i.e., the ratio of $G(t)$ to that estimated at extraterrestrial level $G_{ext}(t)$:

$$k_c(t) = \frac{G(t)}{G_{ext}(t)} \tag{4}$$

$$G_{ext}(t) = G_{SC}\,\varepsilon(t)\sin h(t) \tag{5}$$

where G_{SC} is the solar constant, $\varepsilon(t)$ is the eccentricity correction factor according to Ref. [37], and $h(t)$ is the solar elevation angle.

And the DASSN is defined as [24,25]:

$$DASSN = \frac{1}{T}\sum_{t=1}^{T-1} \zeta(t) \tag{6}$$

$$\zeta(t) = \begin{cases} 1, & if \;\; \xi(t+1) > \xi(t) \\ 0, & otherwise \end{cases} \tag{7}$$

where $\xi(t)$ is the sunshine number, a binary variable indicating whether the sun is covered, quantitatively defined as:

$$\xi(t) = \begin{cases} 1, & if \;\; \frac{G_d(t)}{\sin h(t)} > G_{thr} \\ 0, & otherwise \end{cases} \tag{8}$$

where $G_d(t)$ is the direct normal irradiance, and G_{thr} is an artificial threshold of 120 $\mathrm{W/m^2}$, consistent with the criteria for sunshine duration [38]. In this study, we use GHI data as a substitute due to the lack of high-quality direct normal irradiance data. As for G_{thr}, instead of setting an arbitrary value, a sequence of values (120, 240, 360, 480, 600, and 800 $\mathrm{W/m^2}$) are used to test the robustness of this index.

3. Results

In this section, SII is first elaborated upon through case studies, followed by an exploration of its interactions with GHI, temperature, and humidity. Finally, a comparative analysis with DARR and DASSN is presented to emphasize SII's superior correlation with PV power output.

3.1. Comprehension of SII

To facilitate the comprehension of SII, we initiate a case-based explanation of its functioning. Fig. 2a illustrates the diurnal cycle of GHI, which is obtained from smoothed original annual mean GHI. This cycle exhibits a clear symmetric pattern, with irradiance rising steadily from 6 a.m. at sunrise, peaking around noon at approximately 550 $\mathrm{W/m^2}$, and then declining to zero around 6 p.m. during sunset. On specific days, variations in solar irradiance introduce noise into the diurnal cycle, showcasing different frequency components. For instance, on September 12, GHI evolution exhibits a predominantly gentle pattern but undergoes a sharp drop after 1 p.m., indicating significant low-frequency variations (Fig. 2b). Conversely, on July 19, the GHI time series follows the diurnal cycle but displays pronounced jagged noise, reflecting substantial high-frequency variations (Fig. 2c). As a metric for measuring the minimal "cost" of adjusting the intra-day

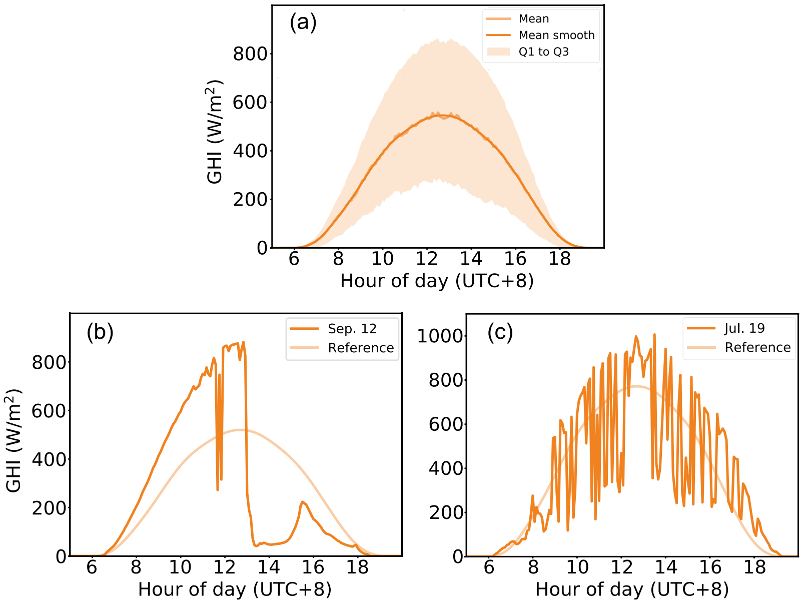

Fig. 2. Diurnal variation of global horizontal irradiance (GHI, units: $\mathrm{W/m^2}$): (a) annual mean (semi-transparent line), its smoothing using a low-band pass filter (thick line), and the range between the 1st and 3rd quartiles (shaded) for the year 2022; (b) on September 12, 2022 (thick line) and the reference distribution (semi-transparent line, multiplied by the summation of the GHI within the day); (c) similar to (b) but for July 19, 2022.

GHI temporal distribution to match the diurnal cycle (akin to the labor input in earth-moving work), SII is expected to be higher in the first case. Indeed, SII is quantified as 1.25 for the first case and 0.31 for the second case, illustrating that GHI in the first case is far less stable than in the second one.

Additionally, high SII values are also observed on March 22, where both high- and low-frequency variations are present, yielding an SII of 1.29, comparable to September 12 (Figure S1). However, this does not necessarily mean that low-frequency variations always dominate SII values. Instead, SII is primarily influenced by loss in solar resource rather than the frequency of perturbations (Figure S2). Since low-frequency variations frequently result in significant solar resource losses due to prolonged reductions in GHI, they typically lead to higher SII values. This underscores the critical role of low-frequency variations in predicting solar resource losses and highlights the need for solar irradiance instability quantifiers that can effectively capture these variations.

3.2. Physical processes regarding SII

Fig. 3 provides the daily evolution of SII, GHI, RH, and temperature over a year. It is revealed that SII ranges from 0 to 2.5 without a discernible seasonality. On the contrary, GHI and temperature demonstrate a clear seasonality, with values higher in summer (July to August) than in winter (December to February), corresponding to the evolution of solar elevation angle. Notably, the inter-day variability is more pronounced than seasonality for GHI, but the seasonality dominates the overall fluctuation for temperature. Regarding RH, no seasonality is observed; however, marked fluctuations are noted from October to December. These fluctuations are primarily attributed to two strong cold anticyclone events (which hinder the flow of moist air, leading to a drier local environment), as corroborated by meteorological records.

From Fig. 3, it can be found that high values of SII typically coincide with low values of GHI, a relationship further substantiated by a correlation coefficient of −0.51 ($p < 0.01$), as shown in Table 1. This inverse relationship results from the nature of SII, which quantifies the deviation of GHI distribution from the diurnal cycle. Generally speaking, a high SII indicates a substantial loss in solar resource. The loss of solar resource is primarily due to synoptic weather events involving moist processes (which are fundamental to cloud formation and precipitation) that frequently block solar radiation through cloud cover. This assertion is supported by the negative correlation between GHI and RH ($r = -0.38$, $p < 0.01$, shown in Table 1), for that elevated RH usually coincides with active moist processes. As such, active moist processes also lead to a high level of solar irradiance instability, evidenced by the correlation coefficient between SII and RH being 0.38 ($p < 0.01$).

Table 1
Pearson correlation coefficients of solar instability index (SII) and global horizontal irradiance (GHI), and their respective correlation coefficients with relative humidity (RH) and temperature. The daily values for all variables except SII are obtained by taking their daily mean.

Variable	Corr with SII	Corr with GHI
SII	/	−0.51*
GHI	−0.51*	/
RH	0.38*	−0.38*
Temperature	0.033	0.45*

* Indicates $p < 0.01$ in a two-tailed student's t-test.

Despite GHI's strong correlation, SII does not exhibit clear relationship with temperature (Fig. 3, Table 1). From a statistical perspective, the correlation between GHI and temperature arises from their shared seasonality. Since seasonality primarily influences temperature variations and inter-day fluctuations primarily influence GHI variations, SII, which lacks seasonality, does not correlate strongly with temperature. However, it may still show some association with GHI due to its sensitivity to daily-scale fluctuations. Consequently, the monthly mean of SII does not correlate strongly with GHI, as the data is dominated by seasonality rather than by daily-scale fluctuations (Table S1, Figure S3). From a physical standpoint, the correlation of GHI and temperature is governed by changes in the solar elevation angle. However, the lack of correlation between SII and air temperature is attributable to the nonlinear relationship between air temperature and synoptic phenomena, especially those encompassing moist processes, which are responsible for significant deviation of GHI to the diurnal cycle.

In summary, this analysis unveils significant correlations of SII with RH and GHI, yet SII demonstrates no clear association with air

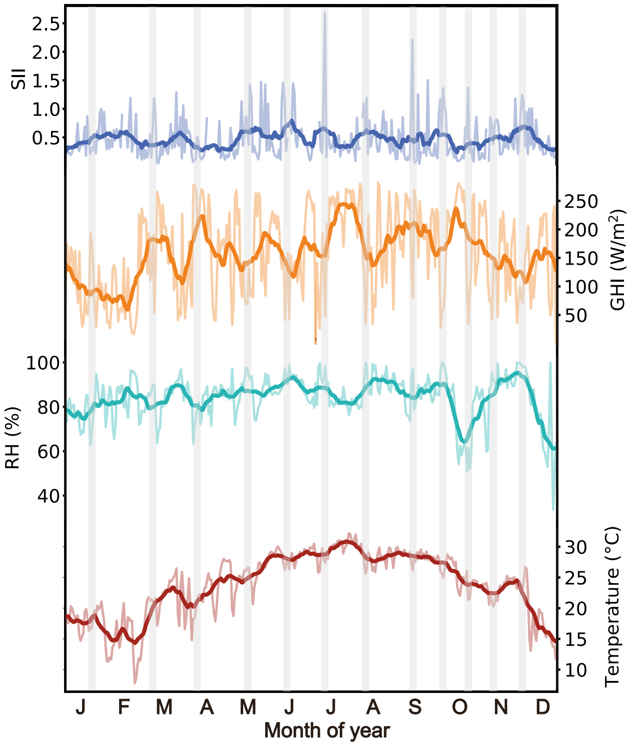

Fig. 3. Evolution of solar instability index (SII), global horizontal irradiance (GHI, units: $\mathrm{W/m^2}$), relative humidity (RH, units: %), and temperature (units: °C) in the year 2022. The semi-transparent and thick lines show the original series and smoothed ones by a 15-day moving average, respectively. The shaded belts indicate the time of coherent change of different variables. The daily values for GHI, RH, and temperature are obtained using the daily mean.

temperature. This highlights the influence of synoptic weather events involving moist processes on solar irradiance stability, independent of fluctuations in air temperature. These results suggest a close association between SII and synoptic weather events that result in the loss of solar resource, positioning SII as a link between atmospheric processes and PV power generation.

3.3. Comparison with established metrics

We chose two commonly used metrics with distinct nature, DARR and DASSN, and undertook an inter-comparative analysis of SII with them.

In the daily evolution shown in Fig. 4, the correlation coefficient between SII and DARR is −0.11 ($p > 0.05$), indicating no significant association. In contrast, the correlation coefficient between SII and DASSN, with a threshold of 120 $\mathrm{W/m^2}$, is 0.32 ($p < 0.01$), suggesting a solid positive linkage. Furthermore, a negative correlation of $r = -0.16$ ($p < 0.01$) between DARR and DASSN is shown, illustrating their divergent patterns. This result suggests that a comparable stability classification can be achieved using SII and DASSN under specific threshold conditions, whereas distinct outcomes will be obtained when employing SII and DARR. Moreover, adopting DARR and DASSN for assessment may produce opposing findings.

In further evaluating the correlation between different metrics and daily mean power output (Table 2), SII exhibits a marked negative correlation ($r = -0.46$, $p < 0.01$), owing to that unstable solar irradiance conditions tend to induce solar resource loss and further lead to reduction in PV power generation. DARR displays a positive correlation ($r = 0.29$, $p < 0.01$), probably because overcast days with low DARR commonly have low power outputs. DASSN exhibits a range of correlation coefficients, varying from significantly negative to significantly positive, contingent on the chosen threshold. This is because the DASSN considers only variations around the threshold value. Therefore, with a higher threshold, high-power-output cases are more inclined to exhibit a higher DASSN, whereas low-power-output cases are less prone to indicate a higher DASSN, resulting in a higher correlation coefficient of DASSN versus mean power output, and vice versa.

To gain a more nuanced understanding of the distinctions among SII and other metrics, we focus our analysis on two representative cases: September 12 and July 19. Since different metrics employ distinct units and exhibit varying absolute magnitudes, we employ deciles to enhance comparative assessments across these metrics (Table 3). Due to the strong non-linearity of the threshold-based algorithm, the value of DASSN remains constant across the 1st to 4th deciles and similarly for the 5th and 6th deciles. Therefore, cases with a DASSN of 0.35×10^{-2} or lower are classified as the 1st decile, while those above 0.35×10^{-2} and up to 0.69×10^{-2} fall into the 5th decile category.

On September 12, the GHI gradually rises from sunrise to peak from 12 pm−1 pm, characterized by a swift yet sharp oscillation near noon. Subsequently, at 1 pm, a remarkable plunge takes place, reducing the GHI from its peak to a relatively low level, indicating a synoptic weather event in the region. Following this plunge, the GHI remains below a low level with a slight surge around 4 pm, gradually diminishing until complete attenuation after sunset (Fig. 5a). Evidently, the GHI alterations do not manifest substantial high-frequency variations, but the PDF shape undergoes a pronounced transformation. Consequently, SII, designed to gauge the similarity of the shape with the diurnal cycle, registers a highly elevated value (1.25, 9th decile). However, given the extensive cloud cover persisting for almost half a day, DARR remains relatively low (3.87, 2nd decile), rendering it unable to capture the substantial deviation from the diurnal cycle. This observation aligns with the findings of Ref. [39], who noted that overcast days often exhibit low DARR, akin to clear-sky days. In contrast, DASSN is relatively middle level (0.69×10^{-2}, 5th decile) in this instance, as only a few data points surpass the prescribed criteria, resulting in few changes being accounted for in this metric. Notably, DASSN only considers changes from below a given threshold to above, introducing inherent artificiality and insensitivity to alterations occurring above or below the threshold, such as the abrupt change near noon.

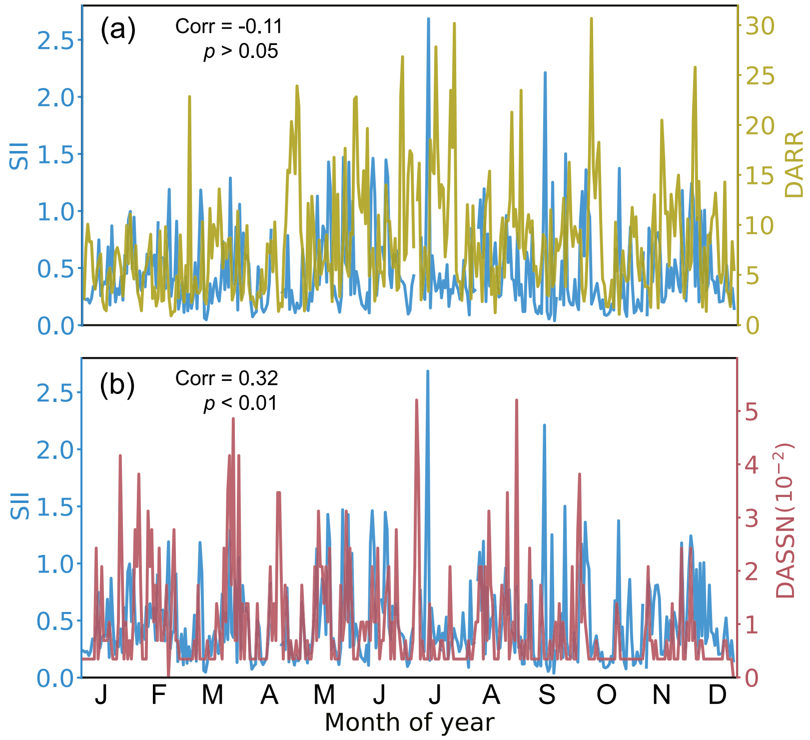

Fig. 4. Daily evolution of solar instability index (SII, in blue color) versus (a) daily aggregate ramp rate (DARR, in gold color) and (b) daily averaged sunshine stability number (DASSN, in red color, multiplied by 10^2) with the threshold of 120 W/m^2 in the year 2022. The Pearson correlation coefficients between the indices and corresponding p values are also shown in the upper left corner of each panel, and the correlation coefficient between DARR and DASSN is −0.16, with $p < 0.01$.

Table 2
Pearson correlation coefficients of solar instability index (SII), daily aggregate ramp rate (DARR), daily averaged sunshine stability number (DASSN), and power output versus each other. The computation of DASSN employs a sequence of thresholds (marked within the parentheses). The daily power output is obtained by taking its daily mean value.

	DARR	DASSN(120)	DASSN(240)	DASSN(360)	DASSN(480)	DASSN(600)	DASSN(800)	Power output
SII	−0.11	0.32*	0.17*	−0.01	−0.09	−0.15*	−0.20*	−0.46*
DARR		−0.16*	0.26*	0.74*	0.87*	0.91*	0.90*	0.29*
DASSN(120)			0.31*	−0.11	−0.22*	−0.27*	−0.31*	−0.54*
DASSN(240)				0.50*	0.27*	0.16*	0.06	−0.23*
DASSN(360)					0.81*	0.70*	0.58*	0.12
DASSN(480)						0.92*	0.79*	0.26*
DASSN(600)							0.90*	0.38*
DASSN(800)								0.48*

* Indicates $p < 0.01$ in a two-tailed student's t-test.

Table 3
The decile value of solar instability index (SII), daily aggregate ramp rate (DARR), and daily averaged sunshine stability number (DASSN). Note that the value of DASSN remains the same from the 1st to 4th deciles and similarly for the 5th and 6th deciles.

Decile	SII	DARR	DASSN(10^{-2})
1	0.13	2.49	0.35
2	0.20	3.47	/
3	0.24	4.60	/
4	0.30	5.56	/
5	0.36	6.89	0.69
6	0.43	8.36	/
7	0.55	9.87	1.04
8	0.70	11.51	1.39
9	0.95	15.43	2.08

However, on July 19, the GHI curve closely adheres to the diurnal cycle but exhibits pronounced high-frequency noise, with a relatively high mean value during daytime (Fig. 5d). Given that the discrepancy of GHI from the diurnal cycle primarily arises from the high-frequency noise, the SII value is 0.31, indicating moderate instability (4th decile). In contrast, for DARR, substantial high-frequency noise leads to significant variations in the clearness index between consecutive time points (Fig. 5e), resulting in a notably high value of DARR (23.48, 9th decile). As a comparison, the DASSN remains at a low level (0.35×10^{-2}, 1st decile) since only sunrise and sunset variations are counted in this case. The GHI during daytime remains higher than the prescribed threshold, and as a result, none of the GHI variations contribute to the DASSN (Fig. 5f).

The analysis reveals that SII excels in capturing low-frequency solar irradiance variations, establishing a robust correlation with PV power output. In contrast, DARR fails to capture prolonged mismatches with the diurnal cycle, while DASSN introduces artificiality as a threshold that must be manually set. As such, SII is a valuable metric for assessing solar irradiance stability compared to these existing metrics in the context of PV power generation.

4. Conclusion and discussion

In this study, we introduce SII as a novel metric for assessing solar irradiance stability. Based on the Wasserstein distance, SII quantifies solar irradiance deviations from the anticipated diurnal cycle, capturing

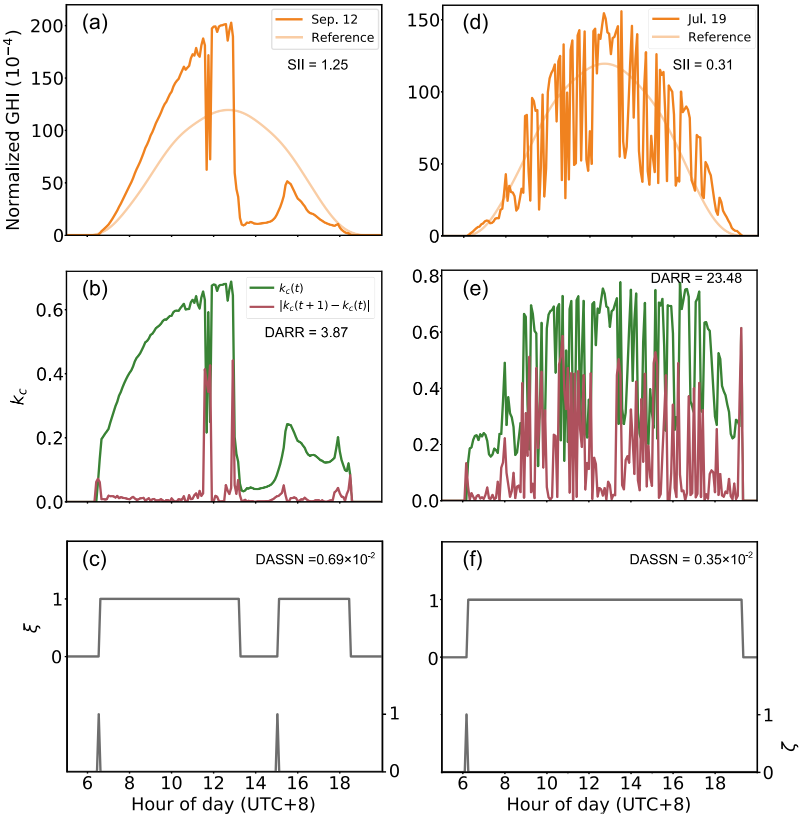

Fig. 5. Evolution of (a) normalized global horizontal irradiance (GHI, thick line) and the reference distribution (semi-transparent line), (b) clearness index ($k_c(t)$, in green color) and the absolute value of its increment ($|k_c(t+1) - k_c(t)|$, in red color), as well as (c) sunshine number (ξ, line in the upper part) and the positive increment of it (ζ, line in the lower part) on September 12, 2022. Similar for (d), (e), and (f), but on July 19, 2022.

both low and high-frequency variations. The physical processes related to SII emphasize the role moist process-involving synoptic weather events in affecting solar irradiance stability. Notably, SII demonstrates a stronger negative correlation with PV power output, outperforming DARR and DASSN, which exhibit limitations in capturing prolonged mismatches with the diurnal cycle and sensitivity to the threshold selection, respectively. Consequently, SII emerges as a valuable tool for assessing the stability of solar irradiance in the context of PV power generation, and offering insights for site selection of PV power plant.

The comparison of various metrics reveals their distinct characteristics. SII captures variations in solar irradiance across both high and low frequencies, thereby providing valuable insights into PV power generation and site selection. In contrast, DARR excels in isolating high-frequency noise in GHI, but may overlook deviations in overcast scenarios. Lastly, while DASSN correlates closely with sunshine duration, its restricted sensitivity to variations above or below the threshold may result in incomplete evaluations of solar resource stability. Therefore, it is essential to choose appropriate metrics based on specific problems.

The findings of our study, based on surface observation data from a humid monsoon region, highlight the pivotal role of moist processes in influencing SII. In this context, cloudiness and precipitation are the primary factors that affect solar radiation stability. While the definition of SII developed in this study is widely applicable, the underlying mechanisms driving SII variations require careful examination in different geographical settings. For instance, it is imperative to reevaluate the significance of these factors when extending our insights to arid or desert regions. In these areas, additional factors like sand storms or dust particles are assumed to be important in shaping dynamics of solar resource, potentially diminishing the impact of moist processes on SII due to prevailing arid conditions. These underscore the importance of region-specific considerations when evaluating the stability of solar irradiance. A broader perspective that accounts for local environmental factors and their impacts on solar irradiance stability is essential for devising accurate strategies to enhance solar energy reliability. Future studies should thus incorporate these diverse influences to craft robust frameworks for assessing stability of solar resource across varying climatic contexts.

CRediT authorship contribution statement

Qun Tian: Writing – original draft, Visualization, Software, Formal analysis, Data curation. **Jinxiao Li:** Writing – review & editing. **Zhiang Xie:** Writing – review & editing, Writing – original draft, Methodology, Conceptualization. **Puxi Li:** Writing – review & editing. **Ya Wang:** Writing – review & editing. **Dongwei Chen:** Writing – review & editing. **Yue Zheng:** Writing – review & editing.

Declaration of Generative AI and AI-assisted technologies in the writing process

During the preparation of this work the authors used ChatGPT-4 in order to improve readability. After using this tool, the authors reviewed and edited the content as needed and took full responsibility for the publication’s content.

Declaration of competing interest

The authors declare that they have no known competing financial interests or personal relationships that could have appeared to influence the work reported in this study.

Acknowledgments

This study was supported by China Postdoctoral Science Foundation Funded Project [grant number: 2023M741531], Shanghai Science and Technology Development Funds, China [grant number: 24QB2703600], Guangdong Meteorological Service Science and Technology Research Project, China [grant number: GRMC2021M01], Guangdong Basic and Applied Basic Research Foundation, China [grant number: 2023A151 5240029], National Key R and D Program of China [grant number: 2021YFC3000904] and the National Natural Science Foundation of China [grant number: 42175105; 42361144708]. We thank Dr. Hongrong Shi for the insightful discussions.

Appendix A. Supplementary data

Supplementary material related to this article can be found online at https://doi.org/10.1016/j.renene.2024.122035.

References

[1] Y. Calisesi, R.-M. Bonnet, L. Gray, J. Langen, M. Lockwood, Solar Variability and Planetary Climates, vol. 23, Springer Science & Business Media, 2007.

[2] M. Wild, D. Folini, C. Schär, N. Loeb, E.G. Dutton, G. König-Langlo, The global energy balance from a surface perspective, Clim. Dyn. 40 (2013) 3107–3134.

[3] G. Kopp, Magnitudes and timescales of total solar irradiance variability, J. Space Weather Space Clim. 6 (2016) A30.

[4] S.K. Solanki, N.A. Krivova, J.D. Haigh, Solar irradiance variability and climate, Annu. Rev. Astron. Astrophys. 51 (2013) 311–351.

[5] G.M. Lohmann, Irradiance variability quantification and small-scale averaging in space and time: A short review, Atmosphere 9 (7) (2018) 264.

[6] D. Yang, W. Wang, C.A. Gueymard, T. Hong, J. Kleissl, J. Huang, M.J. Perez, R. Perez, J.M. Bright, X. Xia, et al., A review of solar forecasting, its dependence on atmospheric sciences and implications for grid integration: Towards carbon neutrality, Renew. Sustain. Energy Rev. 161 (2022) 112348.

[7] R.A. Houze Jr., Cloud Dynamics, Academic Press, 2014.

[8] C.A. Gueymard, Temporal variability in direct and global irradiance at various time scales as affected by aerosols, Sol. Energy 86 (12) (2012) 3544–3553.

[9] S. Mukkavilli, A. Prasad, R. Taylor, A. Troccoli, M. Kay, Mesoscale simulations of Australian direct normal irradiance, featuring an extreme dust event, J. Appl. Meteorol. Climatol. 57 (3) (2018) 493–515.

[10] R. Perez, S. Kivalov, J. Schlemmer, K. Hemker, T. Hoff, Parameterization of site-specific short-term irradiance variability, Sol. Energy 85 (7) (2011) 1343–1353, http://dx.doi.org/10.1016/j.solener.2011.03.016, URL https://www.sciencedirect.com/science/article/pii/S0038092X11000995.

[11] C.J. Smith, J.M. Bright, R. Crook, Cloud cover effect of clear-sky index distributions and differences between human and automatic cloud observations, Sol. Energy 144 (2017) 10–21.

[12] C. Zhang, C. Shen, Q. Yang, S. Wei, G. Lv, C. Sun, An investigation on the attenuation effect of air pollution on regional solar radiation, Renew. Energy 161 (2020) 570–578.

[13] T. Bando, T. Ito, H. Wakisaka, Y. Miyahara, T. Aizawa, T. Harigai, H. Takikawa, M. Hiratsuka, S. Maki, Statistical analysis of cloud layers and solar irradiations for all seasons in Toyohashi city, Japan, Renew. Energy Environ. Sustain. 8 (2023) 18.

[14] M. Lave, J. Kleissl, J. Stein, Quantifying and simulating solar-plant variability using irradiance data, Sol. Energy Forecast. Resour. Assess. (2013) 149–169.

[15] A. Peled, J. Appelbaum, Evaluation of solar radiation properties by statistical tools and wavelet analysis, Renew. Energy 59 (2013) 30–38.

[16] S. Lucaciu, R. Blaga, N. Stefu, M. Paulescu, Quantification of the solar radiative regime variability based on the clearness index, Ann. West Univ. Timisoara Phys. Ser. 59 (2016) 13–17.

[17] V. Badescu, M. Paulescu, Statistical properties of the sunshine number illustrated with measurements from Timisoara (Romania), Atmos. Res. 101 (1) (2011) 194–204, http://dx.doi.org/10.1016/j.atmosres.2011.02.009, URL https://www.sciencedirect.com/science/article/pii/S0169809511000469.

[18] M. Brabec, A. Dumitrescu, M. Paulescu, V. Badescu, A new perspective on the sunshine duration variability, Theor. Appl. Climatol. 139 (2020) 1219–1230.

[19] V.R. da Rocha, R.S. Costa, F.R. Martins, A.R. Gonçalves, E.B. Pereira, Variability index of solar resource based on data from surface and satellite, Renew. Energy 201 (2022) 354–378, http://dx.doi.org/10.1016/j.renene.2022.10.093, URL https://www.sciencedirect.com/science/article/pii/S0960148122015956.

[20] E.W. Luiz, F.R. Martins, A.R. Gonçalves, E.B. Pereira, Analysis of intra-day solar irradiance variability in different Brazilian climate zones, Sol. Energy 167 (2018) 210–219, http://dx.doi.org/10.1016/j.solener.2018.04.005, URL https://www.sciencedirect.com/science/article/pii/S0038092X18303505.

[21] A. Maafi, S. Harrouni, Preliminary results of the fractal classification of daily solar irradiances, Sol. Energy 75 (1) (2003) 53–61.

[22] S. Harrouni, A. Guessoum, A. Maafi, Classification of daily solar irradiation by fractional analysis of 10-min-means of solar irradiance, Theor. Appl. Climatol. 80 (1) (2005) 27–36.

[23] M. Schroedter-Homscheidt, M. Kosmale, S. Jung, J. Kleissl, Classifying ground-measured 1 minute temporal variability within hourly intervals for direct normal irradiances, Meteorol. Z. 27 (2) (2018) 161–179.

[24] R. Blaga, M. Paulescu, Quantifiers for the solar irradiance variability: A new perspective, Sol. Energy 174 (2018) 606–616.

[25] M. Paulescu, V. Badescu, New approach to measure the stability of the solar radiative regime, Theor. Appl. Climatol. 103 (2011) 459–470.

[26] R.L. Dobrushin, Prescribing a system of random variables by conditional distributions, Theory Probab. Appl. 15 (3) (1970) 458–486, http://dx.doi.org/10.1137/1115049, arXiv:https://doi.org/10.1137/1115049.

[27] Y. Robin, P. Yiou, P. Naveau, Detecting changes in forced climate attractors with Wasserstein distance, Nonlinear Process. Geophys. 24 (3) (2017) 393–405, http://dx.doi.org/10.5194/npg-24-393-2017, URL https://npg.copernicus.org/articles/24/393/2017/.

[28] G. Vissio, V. Lucarini, Evaluating a stochastic parametrization for a fast–slow system using the Wasserstein distance, Nonlinear Process. Geophys. 25 (2) (2018) 413–427, http://dx.doi.org/10.5194/npg-25-413-2018, URL https://npg.copernicus.org/articles/25/413/2018/.

[29] G. Vissio, V. Lembo, V. Lucarini, M. Ghil, Evaluating the performance of climate models based on Wasserstein distance, Geophys. Res. Lett. 47 (21) (2020) e2020GL089385.

[30] Z. Xie, D. Chen, P. Li, Discovering climate change during the early 21st century via Wasserstein stability analysis, Adv. Atmos. Sci. 41 (9) (2024) 1–9, http://dx.doi.org/10.1007/s00376-024-3324-6.

[31] M. Muskulus, S. Verduyn-Lunel, Wasserstein distances in the analysis of time series and dynamical systems, Physica D 240 (1) (2011) 45–58.

[32] E. Bernton, P.E. Jacob, M. Gerber, C.P. Robert, On parameter estimation with the Wasserstein distance, Inform. Inference: J. IMA 8 (4) (2019) 657–676.

[33] Q. Yang, P. Yan, Y. Zhang, H. Yu, Y. Shi, X. Mou, M.K. Kalra, Y. Zhang, L. Sun, G. Wang, Low-dose CT image denoising using a generative adversarial network with Wasserstein distance and perceptual loss, IEEE Trans. Med. Imaging 37 (6) (2018) 1348–1357.

[34] S. Chakrabarti, H. Yiming, T. Li, S. Feizi, X. Wu, Quantum Wasserstein generative adversarial networks, Adv. Neural Inf. Process. Syst. 32 (2019).

[35] Y. Dai, S. Wang, X. Chen, C. Xu, W. Guo, Generative adversarial networks based on Wasserstein distance for knowledge graph embeddings, Knowl.-Based Syst. 190 (2020) 105165.

[36] R. Van Haaren, M. Morjaria, V. Fthenakis, Empirical assessment of short-term variability from utility-scale solar PV plants, Prog. Photovolt., Res. Appl. 22 (5) (2014) 548–559.

[37] J. Spencer, Fourier series representation of the position of the sun, Search 2 (5) (1971) 172.

[38] World Meteorological Organization, Guide to Meteorological Instruments and Methods of Observation, Secretariat of the World Meteorological Organization, 2008.

[39] R. van Haaren, M. Morjaria, V. Fthenakis, Empirical assessment of short-term variability from utility-scale solar PV plants, Prog. Photovolt., Res. Appl. 22 (5) (2014) 548–559, http://dx.doi.org/10.1002/pip.2302, URL https://onlinelibrary.wiley.com/doi/abs/10.1002/pip.2302.